Supervised machine learning-assisted current transformer waveform reconstruction for fundamental fault current phasor estimation

Tajdinian, Mohsen; Behdani, Behzad; Popov, Marjan

DOI
10.1016/j.ijepes.2025.111436

Publication date
2025

Document Version
Final published version

Published in
International Journal of Electrical Power & Energy Systems

Electrical Power and Energy Systems 173 (2025) 111436

Contents lists available at ScienceDirect

International Journal of Electrical Power and Energy Systems

journal homepage: www.elsevier.com/locate/ijepes

Supervised machine learning-assisted current transformer waveform reconstruction for fundamental fault current phasor estimation

Mohsen Tajdinian [a], Behzad Behdani [b,*], Marjan Popov [b]

[a] Hitachi Energy Research, Forskargrand 7, Västerås, 72226, Västmanland, Sweden
[b] Delft University of Technology, Faculty of EEMCS, Mekelweg 4, 2628 CD, Delft, The Netherlands

ARTICLE INFO

Keywords:
Current transformer saturation
Least squares
Phasor estimation
Supervised machine learning
Support vector machine (SVM)

ABSTRACT

Deteriorated measurements due to the saturation of current transformers (CTs) are a major challenge in digital power system protection schemes. Failing to resolve this issue effectively can have serious consequences for the accuracy of measured components in phasor-based digital relaying algorithms. Potentially, this may compromise the secure and reliable operation of the protection system and, hence, the entire power system. Accurate fault detection or classification can be achieved by applying an algorithm that can deal with the CT saturation effects. In this paper, a method is presented that can accurately estimate the fundamental current phasor during CT saturation. Reconstruction of the deteriorated measured waveform is accomplished by applying a supervised machine learning algorithm, namely the support vector machine (SVM). The least squares (LS) method is integrated with the SVM-based algorithm to reduce the complexities of waveform reconstruction regressions. A modified discrete Fourier transform (DFT), robust to decaying DC components, is then applied to the reconstructed waveform to extract the required phasor components. The proposed approach is validated by evaluating its classification and phasor estimation performance using standard metrics over numerous simulated cases and field measurements. The results demonstrate the high accuracy of the proposed method to classify different levels of CT saturation and ensure precise estimation of the fundamental phasor component.

1. Introduction

Power system protection against short-circuit (SC) faults profoundly relies on current signal measurements using current transformers (CTs). For ideal operating conditions, a CT is expected to deliver a scaled-down replica of the current passing through its loophole on the secondary side. This is crucial for the reliable operation of protective algorithms applied in digital relays based on intelligent electronic devices (IEDs). Nevertheless, CTs are prone to magnetic core saturation, leading to nonlinear operation and deteriorated measurements, which threaten the protection of the power system. The severity of CT saturation is affected by the asymmetrical fault current level, remanent core flux, and CT burden.

Typically, the phasor measurement algorithms are applied to calculate and estimate the fundamental frequency component from the current delivered on the secondary of the CT. The estimated phasor is an input for the protection and control functions in IEDs. However, according to the aforementioned, CT saturation can cause severe distortions in the secondary current and thus lead to reduced accuracy in estimating the fundamental component. As a result, the issue of CT saturation in digital relays can result in the malfunction of overcurrent protection, distance protection, busbar protection, differential protection, and electric arc detection algorithms for overhead lines [1–10].

The CT saturation detection and waveform reconstruction approaches discussed in the literature can be categorized into three main groups:

- **G1. Model-Based Methods** [5–8]**:** The methods within this category focus on the reconstruction of the CT saturated current by developing a proper CT model. According to [6,7], the CT saturation onset is determined by analyzing the magnetic flux at the saturation inception onset. However, these approaches often struggle with the determination of the saturation starting point and are prone to inaccuracies under noisy conditions.
- **G2. Artificial Intelligence-Based Methods** [9–12]**:** These methods are capable of accurately extracting features in a supervised/unsupervised manner, enabling them to effectively reconstruct and classify varying levels of CT saturation with high precision.

* Corresponding author.
E-mail address: B.Behdani-1@tudelft.nl (B. Behdani).

https://doi.org/10.1016/j.ijepes.2025.111436
Received 15 May 2025; Received in revised form 25 October 2025; Accepted 29 November 2025
Available online 6 December 2025

Table 1
Evaluation of present CT waveform reconstruction methods.

Method		PoV1	PoV2	PoV3	PoV4
G1	[5]	✓	✗	✗	✓
	[6]	✓	✓	✗	✓
	[7]	✓	✗	✗	✓
	[8]	✓	✗	✗	✓
G2	[9]	✗	✗	✗	✓
	[10]	✓	✗	✗	✓
	[11]	✓	✗	✗	✗
	[12]	✓	✗	✗	✓
G3	[13]	✗	✗	✗	✗
	[14]	✗	✗	✗	✓
	[15]	✓	✗	✓	✓
	[16]	✓	✗	✓	✓
	[17]	✓	✗	✓	✓
	[18]	✓	✗	✗	✓
	[19]	✓	✗	✗	✗
	[20]	✓	✗	✗	✓

Although these algorithms show strong classification results by employing hierarchical learning to extract high-level features, they face challenges related to training, feature selection, and problem dimensionality.

G3. Signal Processing Based Methods [13–20]**:** This group of methods deals with defining mathematical relations to extract particular parameters and features from the unsaturated part of the fault current. However, these methods depend on the current waveform and may exhibit inaccuracies due to rapid CT saturation.

In this paper, CT saturation detection and waveform reconstruction are investigated from several points of view (PoV), as follows: **PoV1–** waveform reconstruction capability, **PoV2–** ability to distinguish fault currents from inrush currents, **PoV3–** consideration of CT's dynamic behavior in waveform reconstruction, **PoV4–** sub-cycle response time feasibility. Table 1 provides a summary of the most prominent published studies on CT saturation and waveform reconstruction evaluated according to these PoVs.

As it is stated in Table 1, apart from the methods in [9,13,14], all other methods are capable of CT waveform reconstruction. In addition, the methods in [15–17] perform the waveform reconstruction by taking into account CT's dynamic behavior. Nonetheless, it is worth mentioning that the method in [17] employs a high-order derivative to eliminate the DC component of the fault current signal. The method in [6] can also detect CT saturation and reconstruct the current signal, not only in the case of a fault but also in the case of power transformer inrush currents. As seen in the last column of Table 2, nearly all methods respond within a sub-cycle interval. However, in this case, it is important to consider other PoVs as well. For instance, although the method proposed in [10] performs rapidly, it lacks accuracy due to the absence of capabilities related to PoV2 and PoV3. Furthermore, even though the approach in [20] introduces a one-cycle delay, it demonstrates good accuracy. Hence, maintaining a trade-off between a detailed analysis and operational speed is a key challenge for these methods. The method proposed in [6] performs well and meets the requested trade-off by providing a fast response while maintaining high accuracy. However, this method is limited in application generality due to having a model-based framework.

So far, several artificial intelligence (AI)-based methods have been proposed to serve as classifiers for detecting CT saturation. In [21], saturated and unsaturated CT operation was detected by training an algorithm based on Gaussian Mixture Models (GMMs) using CT secondary current signals under various conditions. However, GMMs are effective only with low-dimensional data and exhibit poor performance with high-dimensional and complex datasets. Furthermore, these models are prone to overfitting because they depend on the supervised classification techniques using manually designed features. A more refined method based on genetic algorithm (GA) application was proposed in [22]. Despite their good performance in optimization problems, the GA-based approaches have often been shown to settle on local optima instead of reaching the global optimum. Moreover, because of their low convergence speed, these algorithms are usually not applicable in real-world situations. The method in [23] employs the particle swarm optimization (PSO) technique for detecting CT saturation in power transformers. In comparison with GAs, PSOs provide more computational efficiency and simplicity in implementation. However, since their global convergence is not secured, and they are susceptible to overfitting, they are not ideal options for classification tasks. In [24], an intelligent algorithm was presented, focusing on the waveform correction distorted by CT saturation. This method, however, does not account for the different levels of saturation (heavy, light, normal). Besides, this algorithm suffers from reliance on manually crafted feature extraction and limited generalization capability. A technique based on decision trees and wavelet transform (WT) was proposed in [25]. The feature extraction in this method is achieved by applying signal processing methods based on wavelet decomposition to the measured differential and restraining currents. With this in mind, it can be indicated that this approach demands considerable signal-processing expertise to ensure meaningful feature extraction.

Driven by the challenges discussed above, this research introduces a hybrid learning-based method to estimate the fundamental phasor component of the fault current under CT saturation. This learning-based technique can reconstruct saturated fault currents and enhance the accuracy of phasor estimation in the case of CT saturation. The main contributions of this paper are summarized as follows:

1. Supervised learning is applied to reconstruct the saturated fault current waveform by considering this task as a time-series prediction problem. This approach combines least squares, support vector machines (LSSVM), and performs the time-series prediction by solving a system of linear equations.
2. Despite its enhanced computation speed, LSSVM still operates as a batch-learning algorithm. In such a framework, for every new data arrival, all the past and current data are retrained. This procedure requires inversion of a larger matrix at each phase, making it computationally expensive and time-consuming. This issue is overcome through an online learning LSSVM using a recursive approach to enable fast current signal prediction.
3. Once the current signal is reconstructed, it is processed through a modified Discrete Fourier Transform (DFT) to eliminate the decaying DC component, ensuring stability and accuracy of estimation. Integrated with LSSVM, this approach achieves accurate phasor estimation within one cycle for any CT saturation level.

This paper is structured as follows: Section 2 elaborates on the proposed approach. Section 3 explains the data collection and necessary preprocessing steps. In Section 4, the performance of the proposed approach is evaluated using simulation and field-recorded data, and comparisons are made with existing methods. Finally, the conclusions are discussed in Section 5.

2. The proposed method

This section provides a detailed description of the proposed CT waveform reconstruction method. The presented analysis comprises three main parts, as illustrated in Fig. 1. As can be seen, the first part is related to data preparation for the proposed algorithm. To this aim, data is first generated by performing simulations on a test power system model in the MATLAB/SIMULINK environment. The results of

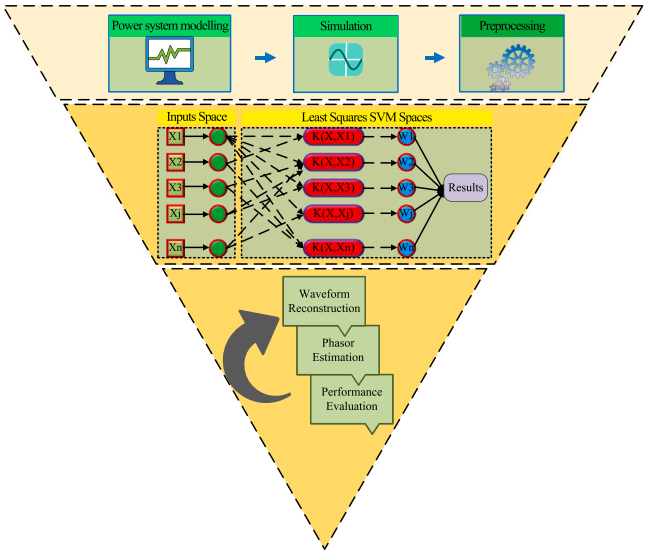

Fig. 1. Structure of the proposed method.

the simulated CT saturation cases are stored in an output file and organized in a preprocessing stage before being fed to the LSSVM algorithm. In the second part, training is performed on the data by applying the LSSVM method as a supervised learning algorithm. The details of the learning method will be explained in the next sections. After the training stage, the built model will be utilized within the phasor calculation algorithm to extract the fundamental phase component of the fault current from the measured data. It is worth mentioning that, since the statistical properties of CT saturation do not change frequently, the LSSVM algorithm is required to be trained only once. Retraining is almost never needed and is only considered in the event of major changes, such as CT replacement or significant system upgrades. In the following, the proposed details of the algorithm are presented.

2.1. The LSSVM algorithm

In the first stage of the proposed CT waveform reconstruction process, the LSSVM algorithm is applied. This algorithm combines the least squares method with the support vector machine. To understand this technique, the training sample set $\{x_k, y_k\}_{k=1}^{n}$ is assumed where $x \in \mathbb{R}^d$ and $y_k \in \mathbb{R}$, with d being the number of input variables. Therefore, the LSSVM regression model is defined as:

$$f(x) = \mathbf{w}^{\mathrm{T}} \psi(x_k) + c\,, \tag{1}$$

where $\mathbf{w}$ denotes the weighting factor, the nonlinear ψ function maps the input variables to a high feature space, and c is the bias factor.

The training data error minimization is carried out with the structural risk minimization (SRM) principle by using the squared errors. As a result, the LSSVM model can be formulated as follows:

$$\begin{aligned} &\min J(\mathbf{w}, e) = \mathbf{w}^{\mathrm{T}}\mathbf{w} + \frac{\eta}{2}\sum_{k=1}^{n} e_k^2 \\ &\text{s.t. } f(x) = \mathbf{w}^{\mathrm{T}}\psi(x_k) + c + e_k\,, \end{aligned} \tag{2}$$

where e_k denotes the $k-$ error variable and η is a penalty factor, defined to provide balance between the model complexity and approximation precision. The optimization problem can be transformed into a system of linear equations by applying the Lagrangian method:

$$\begin{aligned} L(\mathbf{w}, \eta, e, \alpha, c) = &\frac{1}{2}\mathbf{w}^{\mathrm{T}}\mathbf{w} + \frac{\eta}{2}\sum_{k=1}^{n} e_k^2 \\ &+ \sum_{k=1}^{n} \alpha_k \left(r_k - \mathbf{w}^{\mathrm{T}}\psi(x_k)\right) + c + e_k\,, \end{aligned} \tag{3}$$

where k is an integer and α_k denotes the Lagrangian multiplier vector. The optimization of the Lagrangian multiplier method is performed based on the Karush-Kuhn–Tucker (KKT) conditions by setting the kernel function $K(x, x_i) = \psi(x)^{\mathrm{T}}\psi(x_i)$.

Therefore, the LSSVM regression model is obtained as:

$$y(x) = \sum_{k=1}^{n} \alpha_k K(x, x_i) + c\,. \tag{4}$$

2.2. Iterative LSSVM algorithm

Upon training, the LSSVM algorithm can predict the new samples. Method accuracy is proportional to the weighing factors optimally obtained from the performed training. This can slow down the computations of the proposed method, considering that the training stage consumes considerable time. To resolve this issue, instead of retraining, the weighing factors are corrected by the arrival of new samples based on the last prediction error in an iterative manner. By applying this technique, the predictions are obtained based on updated weighing factors.

To implement this iterative approach, the regression model in (4) is modified as:

$$\begin{aligned} y(x) &= \sum_{k=1}^{n} \alpha_k K(x, x_i) + c \\ &= \sum_{k=1}^{n} \varphi_k K(x, x_i) = \mathbf{K}\boldsymbol{\varphi}\,, \end{aligned} \tag{5}$$

where $\mathbf{K}^{+}$ denotes the generalized inverse of $\mathbf{K}$, and $\boldsymbol{\varphi} = \mathbf{K}^{+}(\mathbf{K}\alpha + c)$. It is worth mentioning that while $\boldsymbol{\varphi}$ can get different values, it does not affect the generality of the approach, as expressed in the following.

The kernel function K is considered Gaussian with the standard deviation of σ as:

$$K(x, x_i) = \exp\left(-\|x - x_k\|^2/\sigma^2\right)\,. \tag{6}$$

Now, the value of $\boldsymbol{\varphi}$ can be considered at the initial condition:

$$\boldsymbol{\varphi}_0 = \mathbf{K}_0^{-1} y_0 = \left(\mathbf{K}_0^{\mathrm{T}}\mathbf{K}_0\right)^{-1}\mathbf{K}_0^{\mathrm{T}} y_0\,, \tag{7}$$

where $\mathbf{K}_0$ is the value of the kernel function given by the initial training samples. A regularization parameter is applied to avoid $\mathbf{K}_0^{\mathrm{T}}\mathbf{K}_0$ becoming singular. Therefore, for transforming $\mathbf{K}_0^{\mathrm{T}}\mathbf{K}_0$, the following is enforced:

$$\mathbf{Q}_0 = \mathbf{K}_0^{\mathrm{T}}\mathbf{K}_0 + \frac{1}{R} \quad \text{s.t.} \min\left\{\|\mathbf{K}_0\boldsymbol{\varphi}_0 - y_0 + \frac{\|\boldsymbol{\varphi}_0^2\|}{R}\|\right\}_{\boldsymbol{\varphi}_0}\,. \tag{8}$$

Hence, the following yields:

$$\boldsymbol{\varphi}_0 = \mathbf{Q}_0^{-1}\mathbf{K}_0^{\mathrm{T}} y_0\,. \tag{9}$$

By the arrival of a new sample data, in the first step $\mathbf{K}_1$ is calculated as:

$$\boldsymbol{\varphi}_1 = \mathbf{Q}_1^{-1}\begin{bmatrix}\mathbf{K}_0 \\ \mathbf{K}_1\end{bmatrix}^{\mathrm{T}}\begin{bmatrix}y_0 \\ y_1\end{bmatrix}\,, \tag{10}$$

$$\mathbf{Q}_1 = \frac{1}{R} + \begin{bmatrix}\mathbf{K}_0 \\ \mathbf{K}_1\end{bmatrix}^{\mathrm{T}}\begin{bmatrix}\mathbf{K}_0 \\ \mathbf{K}_1\end{bmatrix} = \mathbf{Q}_0 + \mathbf{K}_1^{\mathrm{T}}\mathbf{K}_1\,. \tag{11}$$

Therefore, the transformation can be written as:

$$\begin{aligned} \begin{bmatrix}\mathbf{K}_0 \\ \mathbf{K}_1\end{bmatrix}^{\mathrm{T}}\begin{bmatrix}y_0 \\ y_1\end{bmatrix} &= \mathbf{K}_0^{\mathrm{T}} y_0 + \mathbf{K}_1^{\mathrm{T}} y_1 = \mathbf{Q}_0\mathbf{Q}_0^{-1}\mathbf{K}_0^{\mathrm{T}} y_0 + \mathbf{K}_1^{\mathrm{T}} y_1 \\ &= \mathbf{Q}_0\boldsymbol{\varphi}_0 + \mathbf{K}_1^{\mathrm{T}} y_1 = \left(\mathbf{Q}_1 - \mathbf{K}_1^{\mathrm{T}}\mathbf{K}_1\right)\boldsymbol{\varphi}_0 + \mathbf{K}_1^{\mathrm{T}} y_1 \\ &= \mathbf{Q}_1\boldsymbol{\varphi}_0 - \mathbf{K}_1^{\mathrm{T}}\mathbf{K}_1\boldsymbol{\varphi}_0 + \mathbf{K}_1^{\mathrm{T}} y_1\,, \end{aligned} \tag{12}$$

and

$$\boldsymbol{\varphi}_1 = \boldsymbol{\varphi}_0 + \mathbf{Q}_1^{-1}\mathbf{K}_1^{\mathrm{T}}\left(y_1 - \mathbf{K}_1\boldsymbol{\varphi}_0\right)\,. \tag{13}$$

Accordingly, for sample k, the following can be calculated:

$$\mathbf{Q}_{k+1}^{-1} = \left(\mathbf{Q}_k + \mathbf{K}_{k+1}^{T}\mathbf{K}_{k+1}\right)^{-1} , \tag{14}$$

$$\boldsymbol{\varphi}_{k+1} = \boldsymbol{\varphi}_k + \mathbf{Q}_{k+1}^{-1}\mathbf{K}_{k+1}^{T}\left(y_{k+1} - \mathbf{K}_{k+1}\boldsymbol{\varphi}_k\right) . \tag{15}$$

The value of $\mathbf{Q}_{k+1}^{-1}$ is obtained by the following approximation as:

$$\mathbf{Q}_{k+1}^{-1} = \left(\mathbf{Q}_k + \mathbf{K}_{k+1}^{T}\mathbf{K}_{k+1}\right)^{-1} = \mathbf{Q}_k^{-1} - \frac{\mathbf{Q}_k^{-1}\mathbf{K}_{k+1}^{T}\mathbf{K}_{k+1}\mathbf{Q}_k^{-1}}{1 + \mathbf{K}_{k+1}\mathbf{Q}_k^{-1}\mathbf{K}_{k+1}^{T}} . \tag{16}$$

By introducing a variable change of $\mathbf{Z}_k = \mathbf{Q}_k^{-1}$, (15) and (16) can be rewritten as:

$$\mathbf{Z}_{k+1} = \mathbf{Z}_k - \frac{\mathbf{Z}_k\mathbf{K}_{k+1}^{T}\mathbf{K}_{k+1}\mathbf{Z}_k}{1 + \mathbf{K}_{k+1}\mathbf{Z}_k\mathbf{K}_{k+1}^{T}} , \tag{17}$$

$$\boldsymbol{\varphi}_{k+1} = \boldsymbol{\varphi}_k + \mathbf{Z}_{k+1}\mathbf{K}_{k+1}^{T}\left(y_{k+1} - \mathbf{K}_{k+1}\boldsymbol{\varphi}_k\right) . \tag{18}$$

In a time-variant system, the operating condition dynamically changes, thus, the output is prone to significant variations. As a result, the prediction model's weighing factors are to be adjusted in proportion to these changes. This can be resolved by introducing *forgetting factors* to the weights in the algorithm. By updating the forgetting factors based on the prediction error, the weights are corrected according to the new arriving data samples [26], as:

$$\boldsymbol{\varphi}_{k+1} = \boldsymbol{\varphi}_k + \frac{\mathbf{Z}_{k+1}\mathbf{K}_{k+1}^{T}}{1 + \gamma_{k+1}}\hat{e}_{k+1} , \tag{19}$$

where $\hat{e}_{k+1} = \left(y_{k+1} - \mathbf{K}_{k+1}\boldsymbol{\varphi}_k\right)$ is the error of new sample from $\boldsymbol{\varphi}_{k+1}$. γ_{k+1} is the update flag, defined as:

$$\gamma_{k+1} = \mathbf{K}_{k+1}\mathbf{Z}_k\mathbf{K}_{k+1}^{T} , \tag{20}$$

where $\gamma_{k+1} = 0$ will result in $\mathbf{Z}_{k+1} = \mathbf{Z}_k$, and in case $\gamma_{k+1} > 0$, Eq. (17) will be changed as:

$$\mathbf{Z}_{k+1} = \mathbf{Z}_k - \frac{\mathbf{Z}_k\mathbf{K}_{k+1}^{T}\mathbf{K}_{k+1}\mathbf{Z}_k}{\xi_{k+1}^{-1} + \gamma_{k+1}} . \tag{21}$$

In (21), ξ_{k+1} is defined as:

$$\xi_{k+1} = \delta_k - \frac{1 - \delta_k}{\gamma_{k+1}} , \tag{22}$$

where $0 < \gamma_k \leq 1$ denotes the forgetting factor, and δ_{k+1} is calculated as:

$$\delta_{k+1} = \left\{ 1 + (1+\varepsilon)\left[\ln\left(1+\gamma_{k+1}\right) + \left(\frac{\left(\tau_{k+1}+1\right)\mu_{k+1}}{1+\gamma_{k+1}+\mu_{k+1}} - 1 \right) \frac{\gamma_{k+1}}{1+\gamma_{k+1}} \right] \right\}^{-1} , \tag{23}$$

where

$$\mu_{k+1} = \frac{\hat{e}_{k+1}^2}{\lambda_{k+1}} ,$$
$$\lambda_{k+1} = \delta_{k+1}\left(\lambda_{k+1} + \frac{\hat{e}_{k+1}^2}{1+\gamma_{k+1}}\right) , \tag{24}$$
$$\tau_{k+1} = \delta_{k+1}\left(\tau_k + 1\right) .$$

Here, the value of ε is fixed, and the initial values of λ and τ are between 0 and 1.

According to the presented relationships, the iterated LSSVM method is given by:

$$\hat{y}_{k+1} = \boldsymbol{\varphi}_{k+1}\mathbf{K}_{k+1} , \tag{25}$$

where $\hat{y}_{k+1}$ corresponds to the calculated prediction. The processing of the LSSVM method is shown in 1.

Algorithm 1 Iterative LSSVM Method

Input: δ_0, λ_0, τ_0, ε, σ, initial dataset $\mathbf{S}_{init}$, and following dataset $\mathbf{S}_{follow}$.
Output: Predicted value $\mathbf{y}$
Initialize: Train the standard LSSVM model by $\mathbf{S}_{init}$ and calculate φ in (5);
Calculate $\mathbf{K}_0$, φ_0, and $\mathbf{Z}_0$ using $\mathbf{D}_{init}$
$k \leftarrow 0$
while $k <$ length($\mathbf{S}_{follow}$) **do**
  Calculate $\mathbf{K}_{k+1}\varphi_{k+1}$, γ_{k+1}, ξ_{k+1} from $(k+1)$-th $\mathbf{S}_{follow}$;
  if $\gamma_{k+1} = 0$ **then**
    $\mathbf{Z}_{k+1} \leftarrow \mathbf{Z}_k$
  else
    $\mathbf{Z}_{k+1} \leftarrow \mathbf{Z}_k - \frac{\mathbf{Z}_k\mathbf{K}_{k+1}^{T}\mathbf{K}_{k+1}\mathbf{Z}_k}{\xi_{k+1}^{-1}+\gamma_{k+1}}$
  end if
  Calculate μ_{k+1}, λ_{k+1} and τ_{k+1};
  $k \leftarrow k+1$;
  $\mathbf{y}_{k+1} \leftarrow \mathbf{K}_{k+1}\varphi_{k+1}$
end while

2.3. Proposed phasor estimation technique

When a fault occurs in the power grid, voltages and currents no longer preserve their standard sinusoidal form. They are affected by waveform distortion and may contain a decaying DC component [27, 28]. The occurred asymmetrical fault current can be expressed by:

$$i(t) = I_{dc}e^{-t/\tau_{dc}} + \sum_{h=1}^{H} I_h \sin\left(2\pi f_0 h t + \theta_h\right) , \tag{26}$$

where $f_0 = 50\,\text{Hz}$ is the power frequency, I_h and θ_h respectively denote the magnitude and phase angle of the hth harmonic component, while I_{dc} and θ_{dc} represent the magnitude and decay time constant of the DC component, respectively.

Typically, the discrete Fourier transform (DFT) is applied in power system protection algorithms to estimate the magnitude and angle of the fundamental phasor component of the fault current, i.e., I_1 and θ_1, by calculating the real and imaginary parts as follows:

$$I_{Re} = \sum_{m=1}^{M} i(m)\sin\left(\frac{2\pi f_0 m T_s}{M}\right) , \tag{27a}$$

$$I_{Im} = \sum_{m=1}^{M} i(m)\cos\left(\frac{2\pi f_0 m T_s}{M}\right) , \tag{27b}$$

where $m = 1, \ldots, M$ denote the samples taken within one cycle with the sampling time of T_s, while $I_1 = \sqrt{I_{Re}^2 + I_{Im}^2}$ and $\theta_1 = \tan^{-1}\left(\frac{I_{Im}}{I_{Re}}\right)$.

Although the DFT algorithm performs well in estimating the desired component and rejecting high-order harmonics, its performance can be significantly degraded by the presence of a decaying DC component. This effect is better understood through Eqs. (28a) and (28b) obtained by substituting (26) in (27a) and (27b).

$$
\begin{aligned}
I_{\mathrm{Re}} &= \sum_{m=1}^{M}\left(I_{\mathrm{dc}}e^{-mT_s/\tau_{\mathrm{dc}}} + I_1\sin\left(2\pi f_0 mT_s+\theta_1\right) + \sum_{h=2}^{H} I_h\sin\left(2\pi f_0 hmT_s+\theta_h\right)\right)\\
&\quad\times\sin\left(\frac{2\pi f_0 mT_s}{M}\right)\\
&= \sum_{m=1}^{M} I_{\mathrm{dc}}e^{-mT_s/\tau_{\mathrm{dc}}}\sin\left(\frac{2\pi f_0 mT_s}{M}\right) + \sum_{m=1}^{M} I_1\sin\left(2\pi f_0 mT_s+\theta_1\right)\\
&\quad\times\sin\left(\frac{2\pi f_0 mT_s}{M}\right)\\
&\quad+\sum_{m=1}^{M}\sum_{h=2}^{H} I_h\sin\left(2\pi f_0 hmT_s+\theta_h\right)\sin\left(\frac{2\pi f_0 mT_s}{M}\right)\\
&= \sum_{m=1}^{M} I_{\mathrm{dc}}e^{-mT_s/\tau_{\mathrm{dc}}}\sin\left(\frac{2\pi f_0 mT_s}{M}\right) + \sum_{m=1}^{M}\frac{I_1}{2}\cos\left(\theta_1\right)\sin\left(\frac{2\pi f_0 mT_s}{M}\right)\\
&\quad= I_{\mathrm{Re}}^{\mathrm{DC}} + I_{\mathrm{Re}}^{\mathrm{Sym}},
\end{aligned}
\tag{28a}
$$

$$
\begin{aligned}
I_{\mathrm{Im}} &= \sum_{m=1}^{M}\left(I_{\mathrm{dc}}e^{-mT_s/\tau_{\mathrm{dc}}} + I_1\sin\left(2\pi f_0 mT_s+\theta_1\right) + \sum_{h=2}^{H} I_h\sin\left(2\pi f_0 hmT_s+\theta_h\right)\right)\\
&\quad\times\cos\left(\frac{2\pi f_0 mT_s}{M}\right)\\
&= \sum_{m=1}^{M} I_{\mathrm{dc}}e^{-mT_s/\tau_{\mathrm{dc}}}\cos\left(\frac{2\pi f_0 mT_s}{M}\right) + \sum_{m=1}^{M} I_1\sin\left(2\pi f_0 mT_s+\theta_1\right)\\
&\quad\times\cos\left(\frac{2\pi f_0 mT_s}{M}\right)\\
&\quad+\sum_{m=1}^{M}\sum_{h=2}^{H} I_h\sin\left(2\pi f_0 hmT_s+\theta_h\right)\cos\left(\frac{2\pi f_0 mT_s}{M}\right)\\
&= \sum_{m=1}^{M} I_{\mathrm{dc}}e^{-mT_s/\tau_{\mathrm{dc}}}\cos\left(\frac{2\pi f_0 mT_s}{M}\right) + \sum_{m=1}^{M}\frac{I_1}{2}\sin\left(\theta_1\right)\cos\left(\frac{2\pi f_0 mT_s}{M}\right)\\
&\quad= I_{\mathrm{Im}}^{\mathrm{DC}} + I_{\mathrm{Im}}^{\mathrm{Sym}}.
\end{aligned}
\tag{28b}
$$

Expressions (28a) and (28b) indicate that the real and imaginary parts of DFT are influenced by the decaying DC component. To eliminate the influence of the decaying DC component on phasor estimation, the following procedure is applied. First, the discrete sum of (26) over one cycle is expressed as:

$$
\bar{I}(m) = \frac{1}{M}I_{\mathrm{dc}}e^{-mT_s/\tau_{\mathrm{dc}}} + \frac{1}{M}\sum_{m=1}^{M}\sum_{h=1}^{H} I_h\sin\left(2\pi f_0 hmT_s+\theta_h\right). \tag{29}
$$

Since the sum of the sinusoidal components over the fundamental period is zero, expression (29) can be simplified as follows:

$$
\bar{I}(m) = \frac{1}{M}I_{\mathrm{dc}}e^{-mT_s/\tau_{\mathrm{dc}}}\left(1-e^{-MT_s/\tau_{\mathrm{dc}}}\right). \tag{30}
$$

The magnitude of the decaying dc component I_{dc} and decay time constant τ_{dc} can be obtained by considering two consecutive samples m and $m+1$ as follows:

$$
\tau_{\mathrm{dc}} = \frac{-T_s}{\ln\left(\frac{\bar{I}(m+1)}{\bar{I}(m)}\right)}, \tag{31}
$$

$$
I_{\mathrm{dc}} = \frac{M\bar{I}(m)}{e^{-mT_s/\tau_{\mathrm{dc}}}\left(1-e^{-MT_s/\tau_{\mathrm{dc}}}\right)}. \tag{32}
$$

Once the parameters of the decaying DC component are calculated, the fundamental phasor component of the fault current can be estimated as:

$$
I_1 = \sqrt{\left(I_{\mathrm{Re}}-I_{\mathrm{Re}}^{\mathrm{DC}}\right)^2+\left(I_{\mathrm{Im}}-I_{\mathrm{Im}}^{\mathrm{DC}}\right)^2}, \tag{33}
$$

$$
\theta_1 = \tan^{-1}\left(\frac{I_{\mathrm{Im}}-I_{\mathrm{Im}}^{\mathrm{DC}}}{I_{\mathrm{Re}}-I_{\mathrm{Re}}^{\mathrm{DC}}}\right). \tag{34}
$$

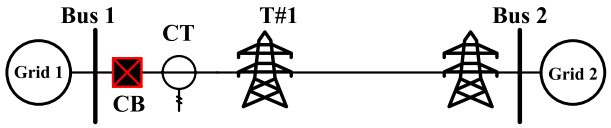

Fig. 2. The test system under study.

Table 2
Specifications of the system under study.

Component	Parameter	Value
AC Source 1	Voltage	138 kV
	Frequency	50 Hz
	Impedance	$R_{\mathrm{th,1}} = 0.3\,\Omega$ $X_{\mathrm{th,1}} = 3.39\,\Omega$
AC Source 2	Voltage	138 kV
	Frequency	50 Hz
	Impedance	$R_{\mathrm{th,1}} = 0.5\,\Omega$ $X_{\mathrm{th,1}} = 4.75\,\Omega$
Transmission Line	Length	50 km
	Sequence Resistance	$R_{\mathrm{L1}} = 6.18\times10^{-3}\,\Omega/\mathrm{km}$ $R_{\mathrm{0,L1}} = 5.447\times10^{-2}\,\Omega/\mathrm{km}$
	Sequence Reactance	$X_{\mathrm{L1}} = 6.24\times10^{-3}\,\Omega/\mathrm{km}$ $X_{\mathrm{0,L1}} = 0.168\,\Omega/\mathrm{km}$
	Sequence Capacitance	$C_{\mathrm{L1}} = 0.0179\,\mu\mathrm{F/km}$ $C_{\mathrm{0,L1}} = 0.0109\,\mu\mathrm{F/km}$

3. Simulation results and discussion

In this section, the performance of the proposed CT waveform reconstruction method is evaluated through simulations using a power system test model, as shown in Fig. 2. In this regard, the test system is simulated by the MATLAB/SIMULINK software package [29], and the simulation results are stored in an output file for further processing. The test system under study includes a 138 kV transmission line, with its terminals connected to Thevenin equivalents of the rest of the network, modeled as AC voltage sources behind impedances. In addition, the standard CT model introduced in [30] is adopted to analyze CT saturation. As implemented in [31], the model provides a balance between simplicity and accuracy. The details of the test system are listed in Table 2.

To generate a comprehensive dataset, numerous simulations are performed by changing parameters such as CT burden, fault type, fault resistance, and CT core remnant flux. The obtained data from the simulations are stored and further analyzed in MATLAB. The sampling frequency is set to 5 kHz considering a sampling rate of 100 samples/cycle under the 50 Hz power frequency. The generated dataset constitutes 4000 cases with various CT saturation levels, i.e., light, normal, and deep. The different CT saturation levels are defined based on the degree of distortion observed in the secondary current waveform [32]. Light saturation refers to conditions where distortion affects less than 10% of the cycle, normal saturation corresponds to distortion lasting between 10%–30% of the cycle, and deep saturation occurs when more than 30%–50% of the cycle is affected.

Therefore, the dataset is divided into two parts: 75 % for training and 25 % for testing, resulting in 3000 training cases and 1000 test cases. The cases are randomly allocated within the two subsets. The developed LSSVM algorithm is implemented to receive CT saturation cases as input and provide a reconstructed waveform as output.

The initial step in training the proposed LSSVM-based CT waveform reconstructor is to adjust the tuning parameters, namely the regularization parameter η in (2) and the kernel parameter σ in (6). The initial training dataset is obtained from a 42-millisecond window comprising one cycle of pre-fault data, 0.1 cycle considered for fault detection

Table 3
Summary of CT saturation cases considered for evaluation.

Case	Level	Cause	Origin
1	light	low decaying DC magnitude	single-phase-to-ground fault (Ag) at $t = 104$ ms
2	normal	moderate decaying DC magnitude	double-phase-to-ground fault (ABg) at $t = 102$ ms
3	deep	high decaying DC magnitude + 50 Ω additional resistive burden	three-phase-to-ground fault (ABCg) at $t = 100$ ms
4	deep	high decaying DC magnitude + 100 Ω additional resistive burden	double-phase-to-ground fault (ABg) at $t = 100$ ms

(to account for the deep CT saturation), and one cycle of post-fault data. The LSSVM parameters (η and σ) are determined using 4-fold cross-validation. Once the optimal values for η and σ are determined, they remain constant throughout the prediction process, and the online rolling prediction of the saturated current is initiated. The prediction starts with a 22 ms window. As new data arrive, the training window is expanded, however, its size is constrained so that the training-to-prediction ratio does not exceed 2:1. Once the prediction window reaches 42 ms, it is fixed at 20 ms. It is essential to note that the ratio and the maximum prediction time window are selected based on a tradeoff between accuracy and the timeliness of the prediction. Here, the algorithm was implemented on a general-purpose workstation-class CPU, and it was observed that the classification and reconstruction of a waveform segment corresponding to a half-cycle (10 ms) required less than 0.8 ms, confirming its real-time feasibility.

3.1. Performance evaluation

As thoroughly discussed in earlier sections, CT saturation can distort the measured current signal, even resulting in a significant deviation from the standard sinusoidal form. To demonstrate the performance of the proposed LSSVM-based CT waveform reconstruction and phasor estimation algorithm, the evaluation is carried out using waveforms from four CT saturation scenarios involving light, normal, and deep saturation conditions. The four considered cases are presented in Table 3, and the performance results of the proposed algorithm, corresponding to the cases in the table, are shown in Figs. 3 to 6. In these figures, the black dashed curves correspond to the actual current at the primary of the CT, the red dashed curves correspond to the measured current transferred to the secondary side of the CT, and the blue curves correspond to the reconstructed waveform obtained from the proposed LSSVM-based algorithm.

The measurement waveforms from Case 1 in Table 3, corresponding to a single-phase-to-ground fault event, are shown in Fig. 3, where the calculated phasor magnitude and angle of the current signal in Fig. 3a are represented in Figs. 3b and c, respectively. As can be seen, the DFT-based algorithm is prone to errors in phasor estimation because of its vulnerability to the decaying DC component caused by CT saturation. Taking the primary signal as a reference, the waveform, magnitude, and phase angle estimated from the uncompensated current exhibit oscillations and a delay of nearly two cycles. In contrast, the proposed algorithm, despite exhibiting a slight initial estimation error due to its dynamic behavior, reconstructs the waveform within one and a half cycles, and achieves a faster and more accurate estimation of magnitude and phase angle compared to the DFT-based method, while maintaining robustness against CT saturation and decaying DC effects.

In Fig. 4, Case 2 from Table 3 is presented, corresponding to a double-phase-to-ground fault that causes normal saturation in the A-phase CT current. Similar to the previous case, the results in Fig. 4 show the vulnerability of the DFT-based algorithm to CT saturation and the decaying DC component. Taking the primary signal as a reference, the waveform, magnitude, and phase angle derived from the uncompensated current exhibit oscillations and a delay of nearly three cycles. In contrast, although an initial estimation error is observed due to the algorithm's dynamic response, the proposed algorithm reconstructs the waveform more accurately within one and a half cycles, and the estimated magnitude and phase angle are significantly less affected by CT saturation and the decaying DC component.

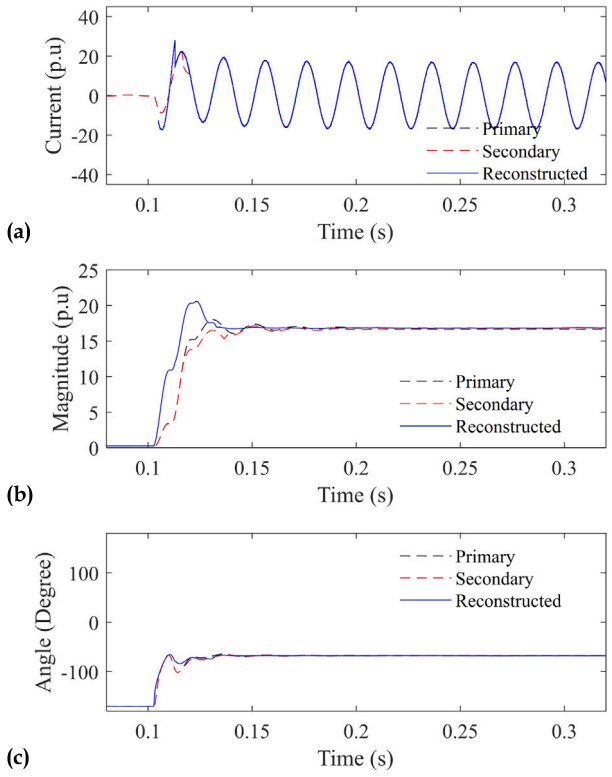

Fig. 3. Simulation results for Case 1 in Table 3: (a) current signal, (b) magnitude, (c) phase angle.

Moving to Case 3, as detailed in Table 3 and illustrated in Fig. 5, this scenario involves a three-phase-to-ground fault combined with an additional burden on the CT secondary, resulting in deep saturation in the A-phase current. Fig. 5 shows that the DFT-based algorithm is significantly affected by CT saturation and the decaying DC component. Using the primary signal as a reference, the waveform, magnitude, and the phase angle obtained from the uncompensated current display oscillations and an approximate delay of four cycles. In contrast, the proposed algorithm effectively reconstructs the waveform within one and a half cycles, and the estimated magnitude and phase angle are much less affected by CT saturation and the decaying DC component.

Finally, Fig. 6 illustrates Case 4 from Table 3, where a two-phase-to-ground fault combined with additional burden in the CT secondary has resulted in deep saturation of the A-phase current. As shown in Fig. 6, the DFT-based algorithm exhibits considerable sensitivity to CT saturation and the decaying DC component. When the primary signal is used as a reference, the waveform, magnitude, and phase angle derived from the uncompensated current waveform show oscillations and nearly four cycles of delay. In contrast, the proposed algorithm reconstructs the waveform within one and a half cycles, and the estimated magnitude and phase angle are less disturbed by CT saturation and the decaying DC component.

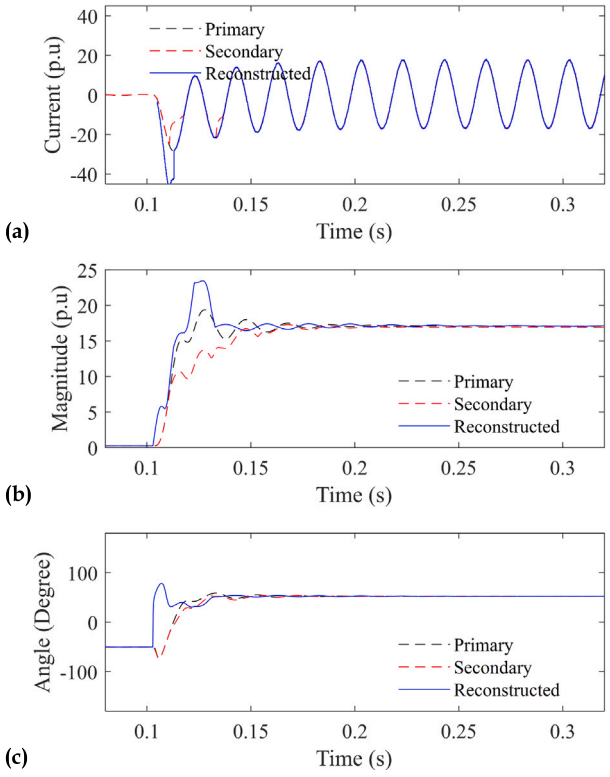

Fig. 4. Simulation results for Case 2 in Table 3: (a) current signal, (b) magnitude, (c) phase angle.

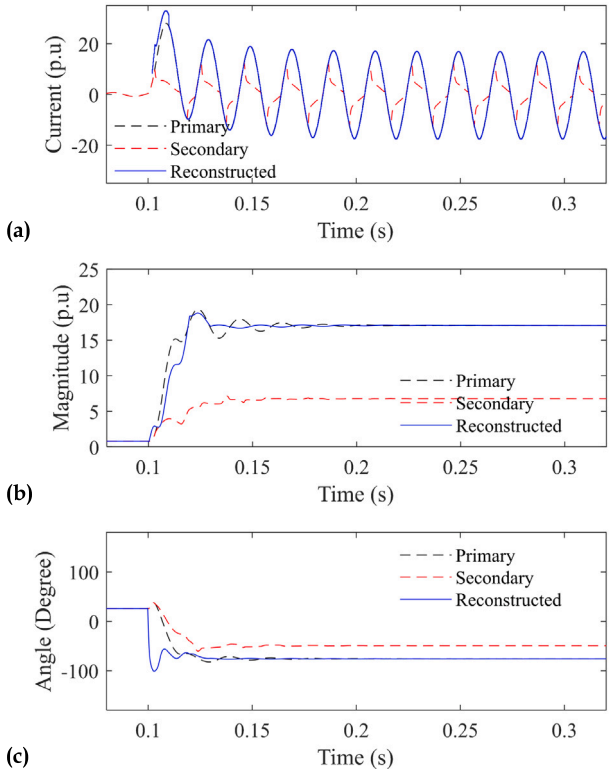

Fig. 5. Simulation results for Case 3 in Table 3: (a) current signal, (b) magnitude, (c) phase angle.

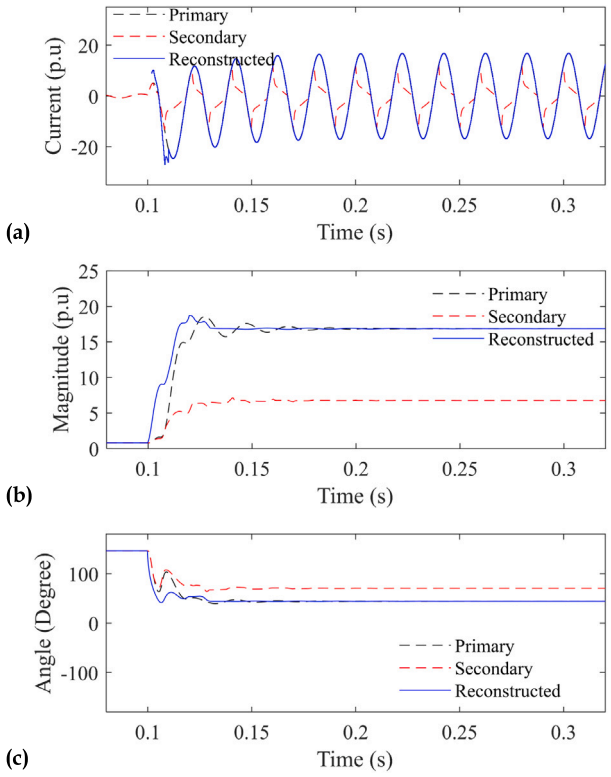

Fig. 6. Simulation results for Case 4 in Table 3: (a) current signal, (b) magnitude, (c) phase angle.

3.2. Execution time and effect of sampling rate

As stated earlier, the timeliness of the prediction is inversely related to the prediction sample rate. While achieving higher accuracy requires a greater number of data points within the prediction window (that is, a higher sampling rate), it is important to reach a tradeoff that ensures satisfactory accuracy while maintaining fast execution time.

To process each window of length W, the proposed method executes three main stages: (i) SVM inference using S support vectors in a d-dimensional feature space, (ii) updating the LS algorithm with k coefficients, and (iii) applying the modified DFT, which is robust against the decaying DC component. In the proposed method, the SVM stage is executed considering $d = W$, and the LS algorithm is updated using a precomputed pseudo-inverse. The SVM inference cost scales as the order of $\mathcal{O}(S \cdot d)$, plus S scalar exponential evaluations for the kernel computations; the LS update requires $\mathcal{O}(k \cdot W)$ operations; and the modified DFT stage operates with a complexity of $\mathcal{O}(W)$. Considering a window length of $W = 20$ samples (corresponding to a 1 kHz sampling rate), a total of $S = 80$ support vectors, and $k = 6$ LS coefficients, the dominant computational cost is associated with the S exponential evaluations in the SVM stage. This leads to a conservative analytical execution time estimate of approximately 0.6 to 1.0 ms per window.

To practically examine the execution time of the proposed method, the LSSVM-based algorithm was implemented on a workstation equipped with a general-purpose CPU (an Intel Core i7 technology here), with 16 GB of RAM. The proposed algorithm is implemented using a pre-allocated, single-thread MATLAB code, intentionally configured in this way to avoid performance optimization, thereby providing a conservative, upper-bound estimate of execution time. The execution time is quantified by processing a number of 20,000 measurement windows and measuring the end-to-end latency in the total runtime. For the chosen sampling rate of 1 kHz, it was observed that processing a window length of 20 samples takes 0.77 ms with a 95 % confidence

Table 4
Effect of sampling rate on execution time of the proposed method.

Sampling rate	Window length – W	No. of support vectors – S	Execution time
1 kHz	20	80	0.77 ms
2 kHz	40	80	1.12 ms
3 kHz	80	100	1.95 ms
4 kHz	100	120	3.42 ms

Table 5
Conditions of Case Studies.

Parameter	Range	Number
FT	LLLG, LLL, LLG, LL, LG	
RF	−60 to 60 %	
SBI	0.5–100 Ω	2000
FIA	0–360°	
SR	20, 100, 200	
Gaussian Noise	40 to 60 dB	

interval of 0.73–0.81 ms. This comfortably fits within the 10 ms half-cycle decision window required at 50 Hz.

In order to characterize the scalability, the execution time of the proposed algorithm is quantified under different sampling rates by processing 20,000 measurement windows for each considered rate. Table 4 summarizes the results obtained for the effect of sampling rate on execution time. As observed in Table 4, even at higher sampling rates, the total execution time remains well below real-time protection constraints.

3.3. Comparison with other methods

The performance of the proposed method (PM) is compared with previously published algorithms. The comparison is conducted for over 2000 fault scenarios for various CT saturation conditions. These conditions are generated by varying the secondary burden impedance (SBI), remnant flux (RF), fault type (FT), and fault inception angle (FIA). Besides, three different sampling rates (SR) are used to evaluate performance under varying resolutions. Gaussian noise corresponding to an SNR range of 40–60 dB is added to the signals during the training and testing stages to reflect realistic CT secondary signal noise. The parameters of the studied cases are summarized in Table 5. The algorithms used for comparison are briefly described below:

- **Method 1 (M1):** The first algorithm is a modified version of the approach presented in [32], which is based on deep learning and fine-tuning optimization. However, this algorithm is designed for the classification of CT saturation rather than compensation. It can detect the saturated interval, and the output serves as a flag indicating the duration of saturation. Then, this flag is combined with a Rogowski coil-based CT saturation compensation method, also introduced in [15]. The platform is implemented in a simulation environment, allowing the secondary current to be extracted using the output from the Rogowski coil during the saturated interval and from the iron-core CT during the unsaturated interval.
- **Method 2 (M2):** The second algorithm is based on a multilayer perceptron (MLP) and is designed to reconstruct the saturated waveform of the CT [33]. The network architecture consists of two hidden layers and one output layer. A data vector with N samples of the saturated current, along with the corresponding primary signal, is used for training.

To evaluate the performance of the considered algorithms, the root mean square error (RMSE) metric is used. The RMSE is calculated over a full cycle of the reconstructed waveform, as defined below:

$$RMSE = \sum_{k=1}^{K} \frac{i_{\text{act}}(t_k) - i_{\text{est}}(t_k)}{K}, \tag{35}$$

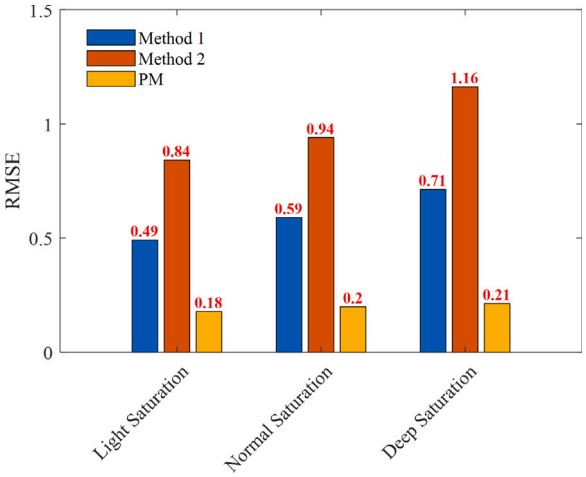

Fig. 7. Performance comparison in terms of RMSE considering different saturation levels.

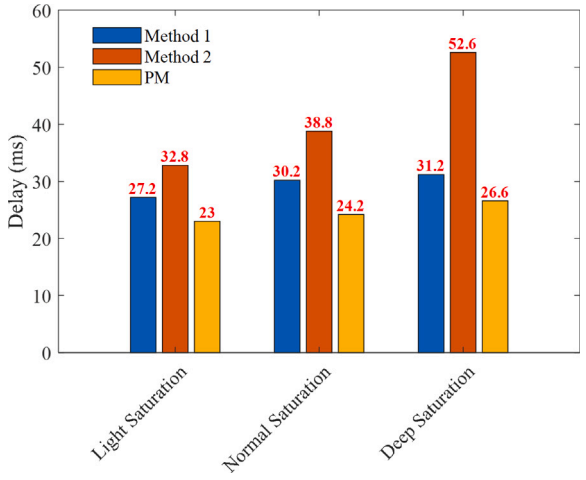

Fig. 8. Performance comparison based on response time delay considering different saturation levels.

where i_{act} and i_{est} denote the *actual* and the *estimated* currents at the kth time sample t_k, with K being the total number of samples in the considered window.

As a first comparison, Fig. 7 shows the average value of the RMSE for each saturation level. It is worth mentioning that for each level of saturation (i.e., light, normal, and deep), 1000 scenarios are considered. As one can see in Fig. 7, the proposed method performs similarly for different levels of saturation, while the performance of the other methods becomes less efficient when they are fed with more distorted waveforms. Moreover, for each class of saturation, the proposed method demonstrates superior performance in terms of RMSE value.

To assess the response time of the PM compared to other methods, the output of each algorithm is applied to the phasor estimation process given in (33) and (34), and the time interval until the phasor reaches a total vector error of less than 2 % is taken as the evaluation metric, i.e. the delay. Fig. 8 shows the average delay for each saturation class. As one can see in Fig. 8, the delay in the proposed method increases by less than 4 ms from light to deep saturation level. The delay increase for Methods 1 and 2 is 4 ms and 20 ms, respectively, indicating that the performance of Method 2 is significantly influenced by the level of CT saturation. Furthermore, as illustrated in Fig. 8, the proposed algorithm exhibits the fastest time response for phasor estimation among all methods.

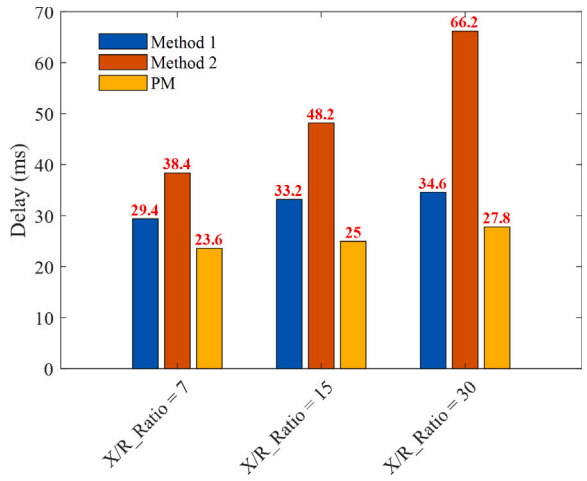

Fig. 9. Performance comparison in terms of response time delay considering different X/R ratios.

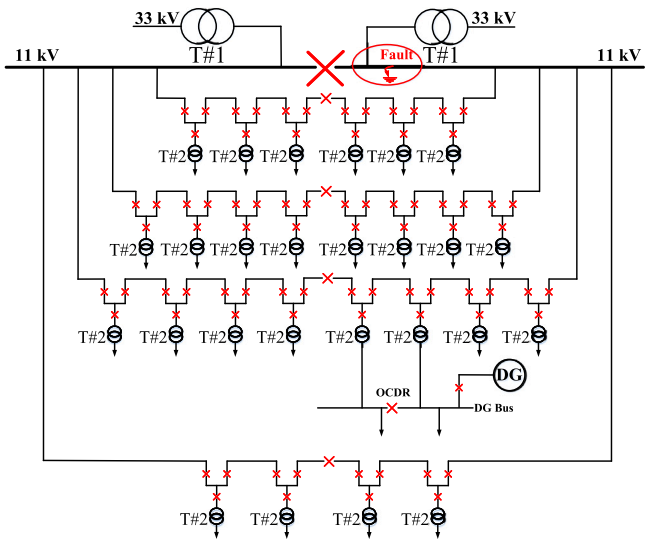

Fig. 10. Single-line schematic of an actual distribution grid with integrated distributed generation (DG) unit.

The ratio of reactance to resistance (X/R) is a factor that influences the presence of decaying DC components in power system fault currents. A higher X/R ratio not only increases the likelihood of deep CT saturation by producing stronger decaying DC components but also introduces potential challenges for phasor estimation. To demonstrate the impact on the algorithms, Fig. 9 shows the phasor estimation time delay for reconstructed waveforms from different algorithms based on 1000 deep CT saturation fault current signals generated for three different X/R ratios.

4. Field recorded data

To demonstrate the effectiveness of the proposed method for real-world conditions, its performance is evaluated using field-recorded data. For this purpose, the proposed algorithm is tested with actual measurement data from the distribution grid of a natural gas liquids refinery plant that processes light hydrocarbons into other compounds, shown in Fig. 10. As shown in Fig. 10, T#1 indicates the incoming transformers rated 33/11 kV, and T#2 marks the low-voltage transformers rated 11/0.4 kV. Most of the connected loads in this network are induction motors. The data is measured from one of the multifunction differential relays protecting the incoming 33/11 kV transformers. This relay measures instantaneous values of fault current and voltage signals at 1 ms intervals (sampling rate of 1 kHz), which corresponds to 20 samples per cycle for the 50 Hz power frequency. The proposed method was implemented on a general-purpose workstation-class CPU. It was observed that the SVM classification and LS-based regression required approximately 0.65 ms to reconstruct a waveform segment of one full cycle, while the modified DFT phasor extraction took around 0.12 ms. Consequently, the total time required for waveform reconstruction and phasor extraction over one cycle is approximately 0.77 ms. This confirms that the proposed method operates an order of magnitude faster than real-time processing requirements.

The performance of the proposed algorithm with field-recorded data is presented in Fig. 11. The results indicate that the DFT-based method is highly sensitive to CT saturation and the presence of decaying DC. When the primary signal is taken as reference, the waveform, magnitude, and phase angle estimated from the uncompensated current show clear oscillations and a delay of nearly two cycles. Furthermore, the proposed method can reconstruct the waveform within one and a half cycles, and the corresponding magnitude and phase angle are less affected by CT saturation and decaying DC components.

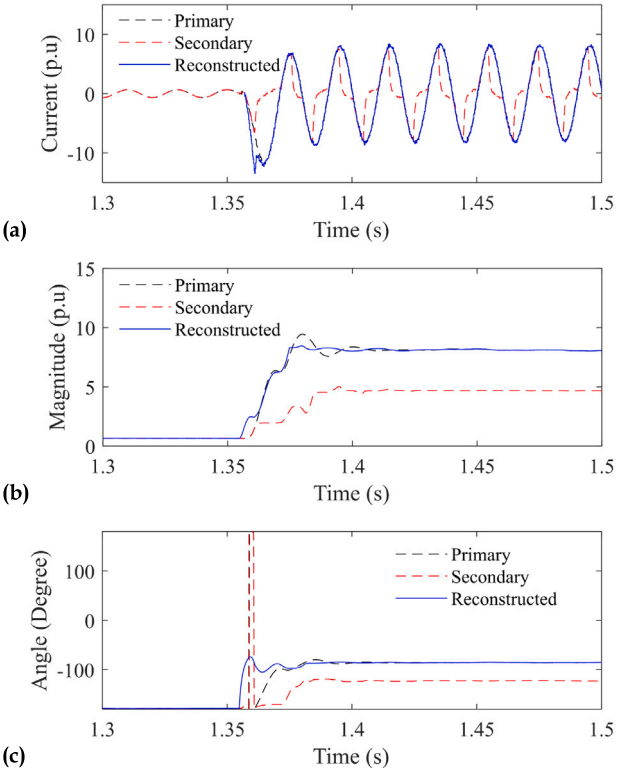

Fig. 11. Simulation results for field-recorded data: (a) current signal, (b) magnitude, (c) phase angle.

5. Conclusions

Distorted waveforms due to CT saturation present a significant challenge to protective relay measurement units and can compromise the overall reliability and security of protection systems. To mitigate this issue, a supervised learning-assisted phasor estimation algorithm was proposed in this study. The proposed framework first utilizes the LSSVM as a regression tool to reconstruct the fault current from the

saturated waveform. Compared to the state-of-the-art methods, the proposed algorithm can reconstruct signals under varying levels of CT saturation, considering different sampling rates, noise levels, fault inception angles, and fault types. For all test scenarios, the reconstruction error was limited to 1.5 %, with the response time confined to one cycle.

Subsequently, a DC-immune DFT was used to extract the phasor component from the reconstructed waveform. The phasor estimation error remained below 1.2 %, with a response time from 20 to 30 ms, excluding the time required for fault detection. Field-recorded data was also used for further validation of the practical applicability of the proposed approach. Among the compared algorithms, the proposed method achieved the best response time for waveform reconstruction and phasor estimation. As the method outperforms existing techniques, future work should focus on integrating classification capabilities to facilitate autonomous identification of CT saturation and fault events. Furthermore, the real-time performance of the proposed algorithm should be evaluated using real-time simulator hardware.

CRediT authorship contribution statement

Mohsen Tajdinian: Writing – review & editing, Writing – original draft, Validation, Software, Methodology, Investigation, Formal analysis, Data curation, Conceptualization. **Behzad Behdani:** Writing – review & editing, Writing – original draft, Visualization, Investigation, Formal analysis. **Marjan Popov:** Writing – review & editing, Writing – original draft, Supervision.

Declaration of competing interest

The authors declare that they have no known competing financial interests or personal relationships that could have appeared to influence the work reported in this paper.

Acknowledgments

This research work has been financially supported by the Nederlandse Organisatie voor Wetenschappelijk Onderzoek (NWO) in collaboration with TSO TenneT, DSO Alliander/Qirion, Royal SMIT Transformers B.V., and TSO National Grid, UK, under the project "Protection of Future Power System Crucial Components (PRoteuS)", No. 18699. Additionally, the contribution from Hitachi Energy Research is highly acknowledged.

Data availability

Data will be made available on request.

References

[1] Wu QH, Lu Z, Ji T. Protective relaying of power systems using mathematical morphology. London, England: Springer; 2009.
[2] Hooshyar A, Afsharnia S, Sanaye-Pasand M, Ebrahimi BM. A new algorithm to identify magnetizing inrush conditions based on instantaneous frequency of differential power signal. IEEE Trans Power Deliv 2010;25(4):2223–33, [Online]. Available: https://ieeexplore.ieee.org/document/5411925.
[3] Naghizadeh RA, Vahidi B, Hosseinian SH. Modelling of inrush current in transformers using inverse Jiles2013Atherton hysteresis model with a neuro-shuffled frog-leaping algorithm approach. IET Electr Power Appl 2012;6(9):727. http://dx.doi.org/10.1049/iet-epa.2012.0085.
[4] Oliveira LMR, Cardoso AJM. Extended park2019s vector approach-based differential protection of three-phase power transformers. IET Electr Power Appl 2012;6(8):463. http://dx.doi.org/10.1049/iet-epa.2011.0377.
[5] Ozgonenel O. Correction of saturated current from measurement current transformer. IET Electr Power Appl 2013;7(7):580–5. http://dx.doi.org/10.1049/iet-epa.2013.0105.
[6] Hajipour E, Vakilian M, Sanaye-Pasand M. Current-transformer saturation compensation for transformer differential relays. IEEE Trans Power Deliv 2015;30(5):2293–302, [Online]. Available: https://ieeexplore.ieee.org/abstract/document/7057675.
[7] Kang YC, Lim UJ, Kang SH, Crossley PA. Compensation of the distortion in the secondary current caused by saturation and remanence in a CT. IEEE Trans Power Deliv 2004;19(4):1642–9, [Online]. Available: https://ieeexplore.ieee.org/document/1339327.
[8] Lu Z, Smith JS, Wu QH. Morphological lifting scheme for current transformer saturation detection and compensation. IEEE Trans Circuits Syst I, Regul Pap: A Publ IEEE Circuits Syst Soc 2008;55(10):3349–57, [Online]. Available: https://ieeexplore.ieee.org/document/4497923.
[9] Rebizant W, Bejmert D. Current transformer saturation detection with genetically optimized neural networks. In: 2005 IEEE Russia power tech. IEEE; 2005, p. 1–6.
[10] Erenturk K. ANFIS-based compensation algorithm for current-transformer saturation effects. IEEE Trans Power Deliv 2009;24(1):195–201, [Online]. Available: https://ieeexplore.ieee.org/document/4696013.
[11] Hong Y-Y, Chang-Chian P-C. Detection and correction of distorted current transformer current using wavelet transform and artificial intelligence. IET Gener Transm Distrib 2008;2(4):566–75. http://dx.doi.org/10.1049/iet-gtd:20070383.
[12] Khorashadi-Zadeh H, Sanaye-Pasand M. Correction of saturated current transformers secondary current using ANNs. IEEE Trans Power Deliv 2006;21(1):73–9, [Online]. Available: https://ieeexplore.ieee.org/document/1564183.
[13] Ji T, Shi M, Li M, Zhang L, Wu Q. Current transformer saturation detection using morphological gradient and morphological decomposition and its hardware implementation. IEEE Trans Ind Electron (1982) 2017;64(6):4721–9, [Online]. Available: https://ieeexplore.ieee.org/document/7864364.
[14] Hooshyar A, Sanaye-Pasand M. Waveshape recognition technique to detect current transformer saturation. IET Gener Transm Distrib 2015;9(12):1430–8. http://dx.doi.org/10.1049/iet-gtd.2014.1147.
[15] Bagheri A, Allahbakhshi M, Behi D, Tajdinian M. Utilizing rogowski coil for saturation detection and compensation in iron core current transformer. In: 2017 Iranian conference on electrical engineering. ICEE, IEEE; 2017, p. 1066–71.
[16] Behi D, Allahbakhshi M, Bagheri A, Tajdinian M. A new statistical-based algorithm for CT saturation detection utilizing residual-based similarity index. In: 2017 Iranian conference on electrical engineering. ICEE, IEEE; 2017, p. 1072–7.
[17] Chothani NG, Bhalja BR. New algorithm for current transformer saturation detection and compensation based on derivatives of secondary currents and Newton2019s backward difference formulae. IET Gener Transm Distrib 2014;8(5):841–50. http://dx.doi.org/10.1049/iet-gtd.2013.0324.
[18] Ji TY, He Q, Shi MJ, Li MS, Wu QH. CT saturation detection and compensation using mathematical morphology and linear regression. In: 2016 IEEE innovative smart grid technologies - Asia. ISGT-Asia, IEEE; 2016, p. 1054–9.
[19] Haghjoo F, Pak MH. Compensation of CT distorted secondary current waveform in online conditions. IEEE Trans Power Deliv 2016;31(2):711–20, [Online]. Available: https://ieeexplore.ieee.org/document/7131537.
[20] Hooshyar A, Sanaye-Pasand M. Accurate measurement of fault currents contaminated with decaying DC offset and CT saturation. IEEE Trans Power Deliv 2012;27(2):773–83, [Online]. Available: https://ieeexplore.ieee.org/document/6127927.
[21] Haji MM, Vahidi B, Hosseinian SH. Current transformer saturation detection using Gaussian mixture models. J Appl Res Technol 2013;11(1):79–87. http://dx.doi.org/10.1016/s1665-6423(13)71516-5.
[22] Rebizant W, Bejmert D. Current-transformer saturation detection with genetically optimized neural networks. IEEE Trans Power Deliv 2007;22(2):820–7, [Online]. Available: https://ieeexplore.ieee.org/document/4141155.
[23] Moradi A, Alinejad Beromi Y, Kiani K, Moravej Z. Artificial intelligence based approach for identification of current transformer saturation from faults in power transformers. Int J Smart Electr Eng 2014;3:37–46.
[24] Segatto EC, Coury DV. A power transformer protection with recurrent ANN saturation correction. In: IEEE power engineering society general meeting, 2005, vol. 2, IEEE; 2005, p. 1341–6.
[25] Sheng Y, Rovnyak SM. Decision trees and wavelet analysis for power transformer protection. IEEE Trans Power Deliv 2002;17(2):429–33, [Online]. Available: https://ieeexplore.ieee.org/document/997912.
[26] Mendes J, Araújo R, Souza F. Adaptive fuzzy identification and predictive control for industrial processes. Expert Syst Appl 2013;40(17):6964–75. http://dx.doi.org/10.1016/j.eswa.2013.06.057.
[27] Tajdinian M, Jahromi MZ, Mohseni K, Kouhsari SM. An analytical approach for removal of decaying DC component considering frequency deviation. Electr Power Syst Res 2016;130:208–19. http://dx.doi.org/10.1016/j.epsr.2015.09.007.
[28] Tajdinian M, Behdani B, Tanbhir Hoq M, Popov M. Sub-cycle phase angle-oriented algorithm for identifying fault direction in renewable-rich MV distribution grids. IEEE Trans Instrum Meas 2024;73:1–11. http://dx.doi.org/10.1109/tim.2024.3460879.
[29] Mathworks.Com, [Online]. Available: http://mathworks.com.
[30] Lucas JR, McLaren PG, Keerthipala WWL, Jayasinghe RP. Improved simulation models for current and voltage transformers in relay studies. IEEE Trans Power Deliv 1992;7(1):152–9, [Online]. Available: https://ieeexplore.ieee.org/document/108902.

[31] Lin X, Zou L, Tian Q, Weng H, Liu P. A series multiresolution morphological gradient-based criterion to identify CT saturation. IEEE Trans Power Deliv 2006;21(3):1169–75, [Online]. Available: https://ieeexplore.ieee.org/document/1645152.

[32] Ali M, Son D-H, Kang S-H, Nam S-R. An accurate CT saturation classification using a deep learning approach based on unsupervised feature extraction and supervised fine-tuning strategy. Energies 2017;10(11):1830. http://dx.doi.org/10.3390/en10111830.

[33] Saidmurodov B, Odinaev I. Current transformer saturation detection bases on artificial neural networks. J Mod Energy Res 2023;1(1):7–16. http://dx.doi.org/10.56947/jmer.v1i1.2.